Practical Implementation of Critical State Models in FEM

D. Sheng
BSc, MSc, Lic Eng, PhD, Research Fellow
S. W. Sloan
BE, MEngSc, MPhil, PhD, FIEAust, Professor
H.S. Yu
BSc, MSc, DIC, DPhil, Senior Lecturer
The University of Newcastle, NSW, Australia

Summary Practical implementation of critical state models into finite element codes is discussed. Improved algorithms for stress integration and load and time stepping are presented, in order to handle the nonlinearities both in elasticity and plasticity. A new generalised critical state model as well as the model proposed by Yu (1998) is implemented. Both uncoupled and coupled analyses of practical problems are carried out.

1. INTRODUCTION

Implementation of critical state models into finite element methods dates back to the 1970s (Simpson, 1973, Naylor , 1975, Carter *et al.*, 1979). Since then, a number of critical state models have been implemented in both commercial and research finite element codes and a good review was given by Gens and Potts (1988). In uncoupled analyses, the numerical performance of these models is very dependent on the choice of stress integration and load stepping scheme. For coupled analyses, it is necessary to select an appropriate time stepping scheme. As pointed out by Gens and Potts, critical state models are particularly vulnerable to numerical breakdown and it is not easy to predict which solution procedure will prove satisfactory for a particular problem. Robust algorithms that work for different problems, different soil types and different loading conditions are thus sorely needed for practical computations with critical state models.

This paper discusses the implementation of general critical state models using a variety of automatic algorithms that have been developed at the University of Newcastle over the past few years. Particular attention is focused on the algorithms of Sloan (1987) and Sloan *et al.* (1998) for stress integration, Abbo and Sloan (1996) for load-displacement integration in uncoupled analysis, and Sloan and Abbo (1998) for time integration in coupled analysis. Refinements to these algorithms for handling nonlinear elasticity in critical state models is presented. Problems covered include the modelling of drained and undrained triaxial tests, undrained expansion of cylindrical cavity, and drained and undrained loading of a rigid footing. Both uncoupled and coupled analyses is carried out.

2. IMPLEMENTATION

2.1 Tangent and Secant Elastic Modulii

In displacement or mixed displacement-pore pressure finite element codes, the global stiffness matrix is typically formed using the tangential constitutive stiffness matrix. The elastic part of the tangential stiffness matrix corresponds to the elastic stress strain relations, $\mathbf{D}_e$, which, in turn, are a function of the elastic tangential bulk modulus K and the shear modulus G. For critical state models, K is often assumed to be a function of the effective mean stress p' according to

$$K = \frac{\partial p'}{\partial \varepsilon_v^e} = \frac{1+e}{\varkappa} p' = \frac{v\,p'}{\varkappa} \tag{1}$$

where ε_v^e denotes the elastic volumetric strain, e the void ratio, v the specific volume, and $\varkappa$ the slope of unloading-reloading line in a $\ln p'$–v diagram. If Poisson's ratio, μ, is assumed to be constant, then the shear modulus G may be written as

$$G = \frac{3(1-2\mu)K}{2(1+\mu)} = \frac{3(1-2\mu)}{2(1+\mu)} \frac{vp'}{\varkappa} \tag{2}$$

The fact that the tangential bulk modulus, defined by equation (1), becomes zero at zero mean effective stress can cause numerical problems in finite element codes. An appropriate modification of equation (1) is to introduce a minimum effective mean stress $p'_{\min}$, below which the bulk modulus is held constant.

If the stresses pass from an elastic state to a plastic state in an explicit integration scheme, it is necessary to compute the intermediate stress state which lies on the yield surface. This implies that the first task in the integration scheme is to determine if the given strain increment causes plastic yielding. If plastic yielding does occur, and the initial stress state is in the elastic region so that $f(\sigma'_0, \kappa_0) < 0$, then the second task is to find the stresses at the intersection point σ'_i so that $f(\sigma'_i, \kappa_0) = 0$. To determine if the given strain increment causes plastic yielding, an elastic trial stress needs to be computed. Since the elastic deformation is nonlinear for critical state models, using the initial tangential elastic modulus may lead to the wrong conclusion. This is shown in Figure 1 where the elastic stress σ'_e computed using the tangential modulus at σ'_0 is inside the yield surface, but the true stress path passes from an elastic to a plastic state. To avoid this problem, a secant elastic bulk modulus can be used to compute the trial stress.

Integrating equation (1) for p' and ε_v^e gives the following incremental relation

$$\Delta p' = p' \left(\exp\left(\frac{v}{\varkappa}\Delta\varepsilon_v^e\right) - 1\right)$$

where p' is the effective mean stress at σ'_0. By definition, the secant bulk modulus for a given elastic volumetric strain increment $\Delta\varepsilon_v^e$ is then

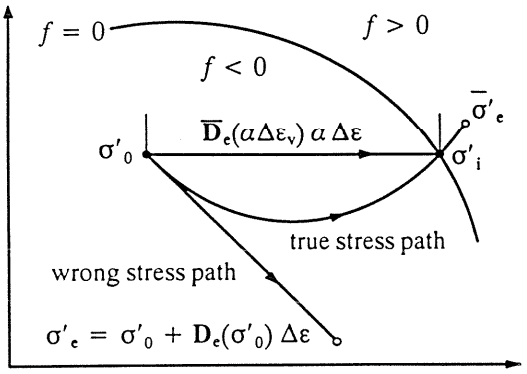

Figure 1. Elastic trial stress by tangential and secant elastic modulii.

$$\bar{K} = \frac{p'}{\Delta\varepsilon_v^e}\left(\exp\left(\frac{\nu}{\kappa}\Delta\varepsilon_v^e\right) - 1\right) \tag{3}$$

At zero elastic volumetric strain, this secant bulk modulus approaches the tangential modulus defined by equation (1).

For a given total strain increment $\Delta\varepsilon$, it can initially be assumed that $\Delta\varepsilon$ is purely elastic. This permits the secant elastic modulus $\bar{K}$ to be computed, using the total volumetric strain increment and the initial effective mean stress, and used to find the correct elastic trial stress state. The task for determining if the given strain increment causes plastic yielding can now be summarised as follows:

1. Enter with a known total strain increment $\Delta\varepsilon$, a known initial stress state σ'_0, and a known initial hardening parameter κ_0.
2. Assume the strain increment is purely elastic and compute the secant bulk modulus $\bar{K}$ using equation (3) and the corresponding shear modulus $\bar{G}$.
3. Compute the secant elastic stiffness matrix $\bar{\mathbf{D}}_e$ using $\bar{K}$ and $\bar{G}$.
4. Compute the elastic trial stress $\bar{\sigma}'_e$ according to
$$\bar{\sigma}'_e = \sigma'_0 + \bar{\mathbf{D}}_e\,\Delta\varepsilon$$
5. If $f(\bar{\sigma}'_e, \kappa_0) \le 0$, the strain increment $\Delta\varepsilon$ is purely elastic. Otherwise, plastic yielding takes place during the strain increment.

If the strain increment $\Delta\varepsilon$ is found to cause a transition of the stress state from elastic to plastic, it is then necessary to locate the intersection point σ'_i with the yield surface. The problem of locating the stresses at the yield surface intersection point σ'_i is equivalent to finding the scalar quantity α which satisfies the nonlinear equation

$$f(\sigma'_i, \kappa_0) = 0 \tag{4}$$

where

$$\sigma'_i = \bar{\mathbf{D}}_e(\alpha\Delta\varepsilon,\ \sigma'_0)\ \alpha\Delta\varepsilon \tag{5}$$

An α value of zero indicates that $\Delta\varepsilon$ is due to purely plastic deformation, while an α value of unity indicates that $\Delta\varepsilon$ is due to purely elastic deformation. Thus, for an elastic to plastic transition, α lies within the range $0 < \alpha < 1$. Note that the elastic secant stiffness matrix in equation (5) is calculated using the initial stress state σ'_0 and the portion of the strain increment $\alpha\Delta\varepsilon$. For a given set of strain increments and initial stresses, the elastic stress increments computed using the corresponding secant stiffness $\bar{\mathbf{D}}_e$ are exact, so that the intersection state σ'_i found according to equation (4) is exact. A fast algorithm for numerical solution of α refers to Sloan *et al.* (1998).

Once the intersection point σ'_i has been found, the standard elastoplastic stiffness matrix $\mathbf{D}_{ep}$, based on the tangential elastic matrix $\mathbf{D}_e$, can be used to find the stress increment corresponding to the strain increment $(1 - \alpha)\Delta\varepsilon$.

2.2 Explicit Stress Integration with Substepping

In the modified Euler stress integration method of Sloan *et al.* (1998), the strain increment is automatically subincremented using a local error estimate for the stresses and hardening parameter at each integration point. This error estimate is formed by taking the difference between a first order accurate Euler solution and a second order accurate modified Euler solution at each stage. The generalised version of this scheme can be summarized as follows.

1. Enter with an initial stress state σ'_0, an initial hardening parameter κ_0, and the strain increment $\Delta\varepsilon$ for the current step.
2. Determine if the strain increment $\Delta\varepsilon$ causes plastic yielding. If no, update the stress state using the elastic trial stress state σ'_e and exit.
3. Find the intermediate stress state σ'_i on the current yield surface and the portion of the strain increment causing plastic deformation. Then set
$$\sigma'_0 = \sigma'_i$$
$$\Delta\varepsilon = (1 - \alpha)\,\Delta\varepsilon$$
The possibility of elastic unloading followed by plastic yielding should be taken into account in this step.
4. Assume that all the strain increment is applied in one step.
5. Compute two sets of stress increments and hardening parameter increments using the Euler method and the modified Euler method, respectively.
6. Compute the relative error based on the difference between the two stress increments and the two hardening parameter increments.
7. If the error is larger than a prescribed tolerance, reduce the strain substep size according to the error and the error tolerance and go to step 5.
8. If the error is within the error tolerance, update the stress state and the hardening parameter using the modified Euler solution. Compute the next strain substep size.
9. If the updated stress state is outside the updated yield surface, project the stress state back to the yield surface.
10. Go to step 5 until the sum of all the strain subincrements equals the total strain increment $\Delta\varepsilon$.

2.3 Load and Time Stepping Schemes

The automatic load stepping scheme by Abbo and Sloan (1996) selects each step so that a local truncation error in the computed deflections is held below a prescribed value. The truncation error is measured by taking the difference between incremental solutions obtained from the first order accurate Euler scheme and the second order accurate modified Euler scheme. The scheme has proven to be particularly robust and permits a broad

class of load-deformation paths to be integrated with only a small amount of drift from equilibrium.

Using a similar philosophy to the load-stepping scheme described above, the adaptive time stepping scheme by Sloan and Abbo (1998) attempts to choose the time subincrements such that, for a given mesh, the time-stepping error in the displacements lies close to a specified tolerance. The local truncation error in the displacements was found by taking the difference between the first order accurate backward Euler solution and the second order accurate Thomas and Gladwell solution.

These two adaptive load and time stepping schemes, however, needs a slight modification for use with critical state models. This is because these models are nonlinear in the elastic range, and it is not possible to to form the elastoplastic global stiffness matrix by subtracting the plastic stiffness terms from the elastic stiffness terms. Instead, the global stiffness matrix must be computed afresh for each step, in the usual way.

3. CRITICAL STATE MODELS

The finite element code, SNAC, has been developed at the University of Newcastle over a number of years (see Abbo, 1997, Abbo and Sloan, 1996, Sloan and Abbo, 1998, Sloan *et al.*, 1998). Originally only conventional elastoplastic models, such as the Mohr-Coulomb, Tresca and Von Mises criteria were implemented, but two critical state (CS) models have now also been incorporated.

The first CS model is developed based on the modified Cam clay (MCC) model (Roscoe and Burland, 1968), with the possibility to overcome the drawback of the MCC model in overestimation of failure stresses on the supercritical side. An associated flow is used and the yield function and the plastic potential take the form

$$f = \frac{1}{\beta^2}\left(\frac{(1+\beta')p'}{p'_0} - 1\right)^2 + \left(\frac{(1+\beta')q}{M(\theta)p'_0}\right)^2 - 1 \tag{6}$$

where β and β' are parameters that adjust the shape of the yield function and the plastic potential as shown in Figure 2. Setting $\beta = \beta' = 1$ in equation (6) leads to the popular modified Cam clay model. The parameter β is always set to 1 on the dry side of the critical state line and $\beta = \beta' \leq 1$ on the wet side of the critical state line.

As another enhancement to the MCC model, the slope of the critical state line, M in equation (6), is expressed as a function of the Lode angle θ, and determines the shape of the failure surface in the deviatoric plane (see Figure 2). During the last two decades, several different functions have been proposed for modelling the shape of the failure surface in the deviatoric plane. An example, due to Zienkiewicz and Pande (1977), may be written as

$$M = \frac{2\alpha M_{\max}}{1 + \alpha - (1-\alpha)\sin 3\theta} \tag{7}$$

where $M_{\max}$ is the slope of critical state line under triaxial compression ($\theta = 30°$). The parameter α can be set to

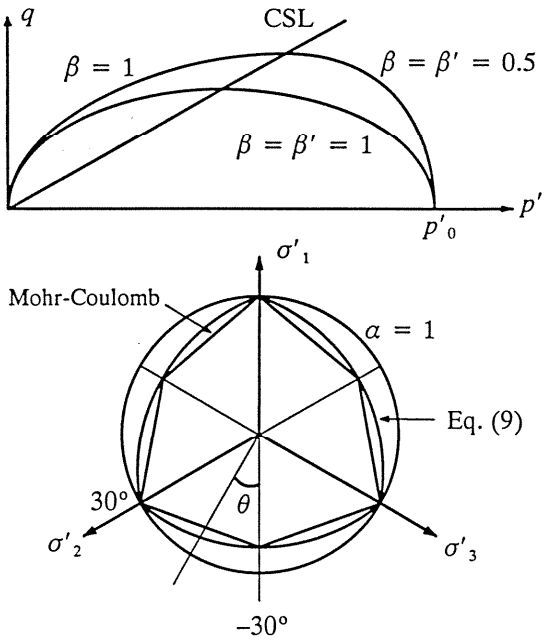

Figure 2. Variation of the yield surface in the generalized Cam clay model.

$$\alpha = \frac{3 - \sin\phi}{3 + \sin\phi} \tag{8}$$

in order to approximate a Mohr-Coulomb failure surface. One problem with equation (7) is that the yield surface is convex only if $\alpha > 0.778$ (ie friction angles $\phi < 22°$). This is obviously not appropriate for most soil types. A better alterative for (7) is suggested here

$$M = M_{\max}\left(\frac{2\alpha^4}{1 + \alpha^4 - (1-\alpha^4)\sin 3\theta}\right)^{1/4} \tag{9}$$

By setting according to equation (8), this yield surface coincides with the Mohr-Coulomb hexagon at all vertices in the deviatoric plane (see Figure 2). Setting $\alpha = 1$ recovers the Von Mises circle. Note that this yield surface is differentiable for all stress states and is convex provided $\alpha \geq 0.6$ (ie for frictional angles in the range $0° \leq \phi \leq 49.6°$)

The second model implemented here is the unified critical state model for clay and sand of Yu (1998). This model uses a non-associated flow rule and its yield function takes the form

$$f = \left(\frac{q}{Mp'}\right)^n + \frac{1}{\ln r}\ln\frac{p'}{p'_0} \tag{10}$$

where n is a parameter used to control the shape of the yield function and r is a spacing ratio used to control the position of the critical state line on the yield surface. If n is set to 1 and r to the natural logarithmic base e in (10), the original Cam clay yield function (Schofield and Wroth, 1968) is recovered.

The plastic potential in Yu's clay and sand model takes the form

$$g = 3M\ln\frac{p'}{\zeta} + (3 + 2M)\ln\left(\frac{2q}{p'} + 3\right) - (3 - M)\ln(3 - q/p') \tag{11}$$

where ζ is a size parameter and is not used in the implementation of the model since only the derivatives of g are needed.

The elastic part of the two classes of critical state models is the same as discussed above, with the tangential bulk modulus defined by equation (1) and the shear modulus by (2). A constant Poisson's ration is used. The hardening law for the two critical state models is also identical. The yield surface size p'_0 is taken as the hardening parameter and is related to the plastic volumetric strain ε_v^p by equation

$$\delta p'_0 = \frac{v\, p'_0}{\lambda - \varkappa}\, \delta\varepsilon_v^p \qquad (12)$$

where λ is the slope of the normal compression line in a $\ln p' - v$ diagram.

4. VERIFICATION AND APPLICATION

In this section, the critical state models described above are used to analyse practical problems. In all analyses in this section, these constitutive laws are integrated very accurately by using a relative local error tolerance of 10^{-6} for the stresses, in conjunction with an absolute tolerance of 10^{-9} for drift from the yield surface. In the analyses with automatic load or time stepping schemes, a displacement tolerance of 10^{-4} is used. In the uncoupled analyses of triaxial tests using the Newton-Raphson scheme, an iteration tolerance of 10^{-6} is used.

4.1 Triaxial tests

Simulation of triaxial tests is one way to verify the implementation of a critical state model. In an ideal triaxial test, the stresses and strains are uniform and thus the computed stresses and strains at each integration point should follow the constitutive relations exactly. To verify this, the popular modified Cam clay model is chosen and the following material parameters are used

$M = 1.2, \lambda = 0.2, \varkappa = 0.02, \mu = 0.3, p'_0 = 60, k = 10^{-8}$

The parameter k is the permeability. The units of these parameters are not important as long as they are all consistent. Two types of initial conditions are considered, respectively representing a slightly overconsolidated soil (NC) and a heavily overconsolidated soil (OC). These are as follows:

NC: $\sigma'_{r0} = \sigma'_{a0} = 50, \quad e_0 = 1.50$
OC: $\sigma'_{r0} = \sigma'_{a0} = 10, \quad e_0 = 1.53$

where σ'_{r0} and σ'_{a0} denote the initial radial and axial stresses, respectively, and e_0 is the void ratio at the initial stress state.

Three different analyses were carried out: an uncoupled elastoplastic analysis with no pore pressures, a coupled analysis of drained compression (with drainage at the ends of the specimen), and a coupled analysis of undrained compression. The first two analyses should produce the same results if the applied strain rate in the coupled analysis is sufficiently small for the particular permeability. For the uncoupled elastoplastic analysis and coupled drained analysis, an axial strain of 50% was imposed in 50 coarse increments. For the coupled undrained analysis, an axial strain of 5% was first applied in 50 increments and an additional 45% in another 50 increments. The time step for the coupled analysis was taken as 10^8 . This guarantees no excess pore pressure in the drained specimen and a uniform excess pore pressure in the undrained specimen.

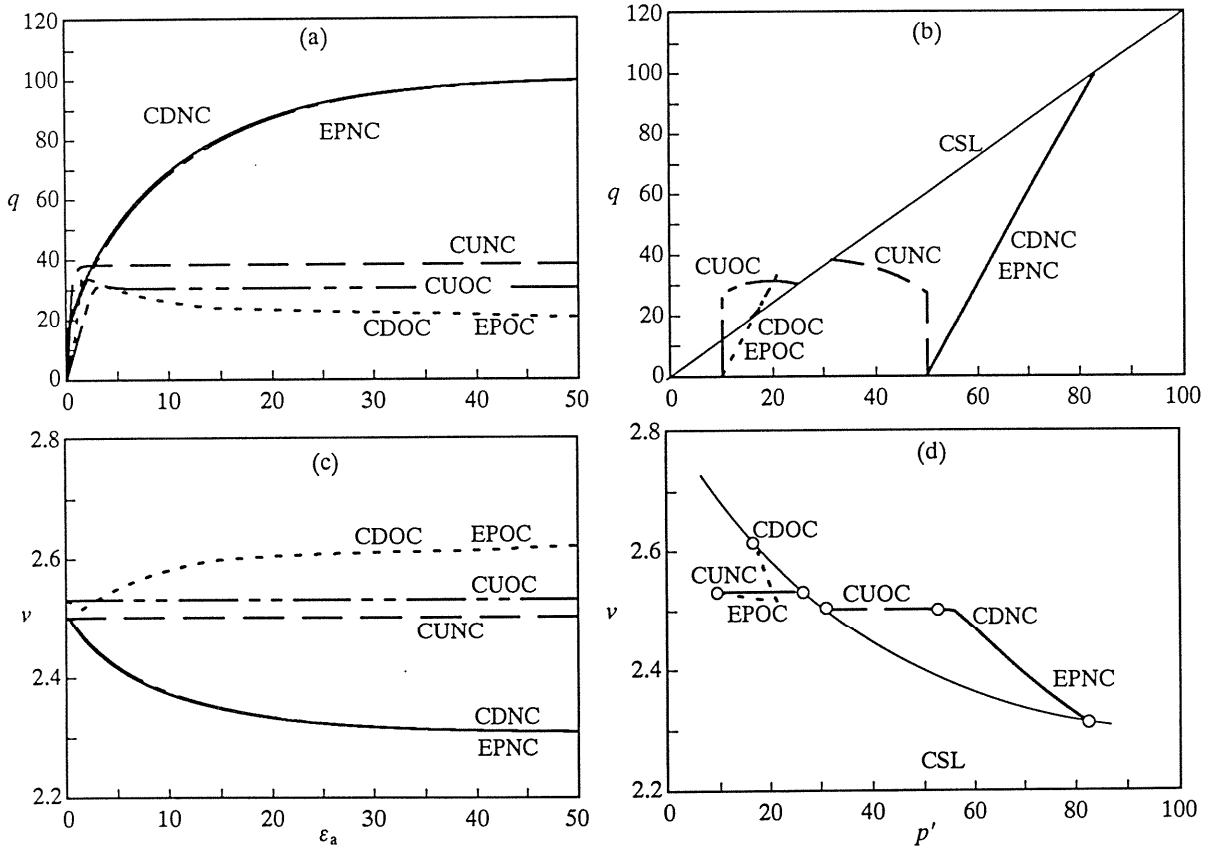

Figure 3. Simulated results for triaxial tests (EP: uncoupled elastoplastic analysis, CD: coupled drained analysis, CU: coupled undrained analysis, NC: normal consolidated soil, OC: overconsolidated soil).

The simulated results, shown in Figure 3, are very close to the theoretical solutions. As expected, the uncoupled elastoplastic analysis and coupled drained analysis produce almost identical results. Hardening of the slightly overconsolidated soil and softening of the heavily overconsolidated soil are well captured. At the end of the applied axial strain, the soil is at the critical state under all the test conditions. In all the analyses, the stresses and strains are found to be uniform within the specimen during the whole range of applied strain.

For this simple example, other stress integration and load and time stepping methods may also produce accurate results if sufficient increments are used. For example, if the same amount of axial strain is applied in 50 increments using the standard Newton-Raphson method, the results obtained are very similar to those shown in Figure 3. However, the total CPU time required for the automatic load stepping scheme is roughly one third of that for the standard Newton-Raphson, even though the number of load subincrements required in the former is larger than the number of iterations in the latter (see Figure 4 and Figure 5). In the automatic scheme, a pronounced

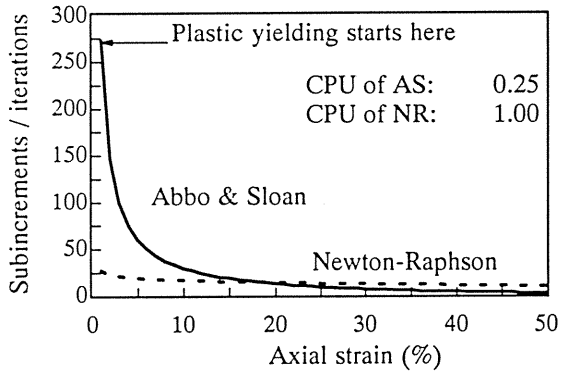

Figure 4. Abbo & Sloan subincrements and Newton-Raphson iteration in uncoupled analysis of NC soil.

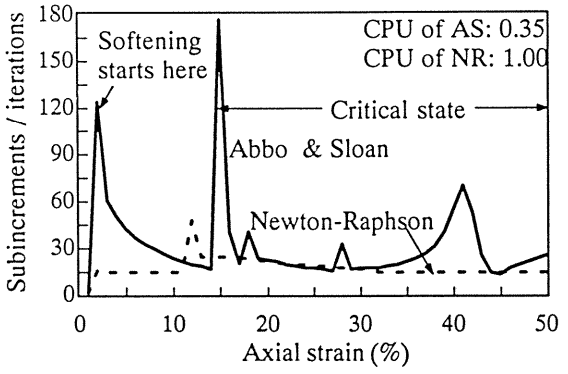

Figure 5. Abbo & Sloan subincrements and Newton-Raphson iterations in uncoupled analysis of OC soil.

increase in the number of load subincrements can be observed whenever the soil yields, softens or reaches the critical state line. The number of iterations for the Newton-Raphson method, on the other hand, is more or less constant over the entire range of axial strain. Another interesting quantity is the average number of strain subincrements required by the automatic stress integration procedure at each Gauss point. The Newton-Raphson method, with 50 increments of fixed size, requires a significantly larger number of strain subincrements than Abbo and Sloan's automatic method (Figure 6 and Figure 7). This is why the Newton-Raphson method requires a larger total CPU time.

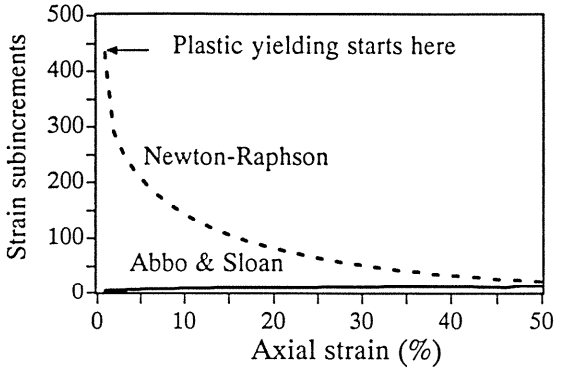

Figure 6. Average strain subincrements in stress integration in uncoupled analysis of NC soil.

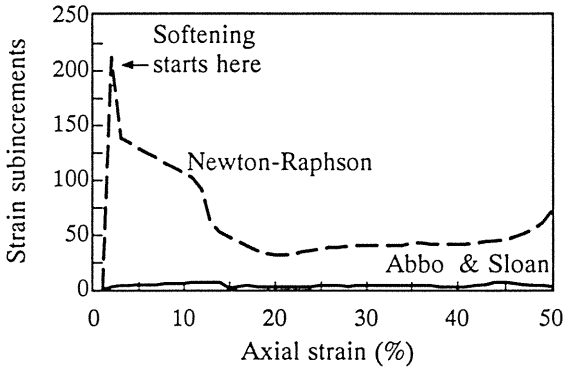

Figure 7. Average strain subincrements in stress integration in uncoupled analysis of OC soil.

4.2 Undrained cylindrical cavity expansion

Analytical solutions for undrained expansion of cylindrical and spherical cavities in soils represented by the original and modified Cam clay models have been obtained by Collins and Yu (1996). These solutions provide another convenient method for verification of the finite element solutions. In this paper, the analytical solution for undrained expansion of a cylindrical cavity will be used to check the numerical solutions of the original Cam clay model.

The analytical solutions obtained by Collins and Yu (1996) assume cavity expansion in an infinite volume. In the finite element analysis, a finite outer radius equal to 20 times the initial cavity radius is used. The initial cavity radius is set to 1. The total radial pressure applied at the outer boundary of the cylinder is kept constant while the total radial pressure applied to the cavity wall increases so that the cavity expands by 50% to a radius of 1.5. This amount of displacement is carried out in 100 increments. All boundaries are sealed for drainage.

The soil parameters used for the original Cam clay are those relevant to London clay. They, as well as initial stresses, can be found in Collins and Yu (1996).

An interesting soil parameter for this problem is the permeability. It is often perceived that, under undrained conditions, the permeability does not influence the

effective stresses or excess pore pressures. This is true only when the undrained condition of zero volume change is satisfied at all local points. However, in a finite element analysis, the condition of no volume change is only guaranteed globally, i.e. only to the whole volume of interest. Due to local drainage, a very large permeability will smooth any gradient in the excess pore pressure and eventually result in a uniform distribution of excess pore pressure. In order to guarantee that the undrained condition is satisfied both globally and locally, a very fast loading is required. In this analysis, the permeability of the soil is set to 10^{-9} and the prescribed radial displacement of 0.5 is applied in a period of 100. Test runs showed that further decrease of the permeability or increase of the loading rate would not lead to any further change in the excess pore pressures.

The numerical and analytical cavity expansion curves are shown in Figure 8. The simulated total radial stress and excess pore pressure at the cavity wall compare well with the analytical values. It is interesting to note that the difference between the total radial stress and the excess pore pressure, i.e. the effective radial stress at the cavity wall, becomes constant after a certain deformation. This state corresponds to the point where the stresses at the cavity wall reach the critical state. This is further confirmed in the stress path diagram.

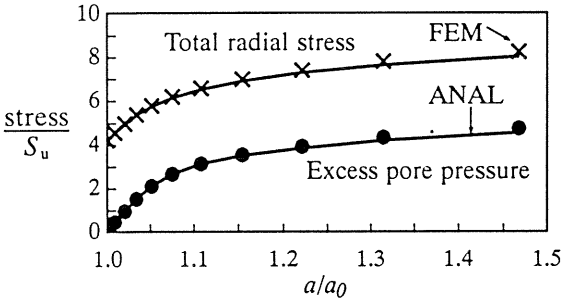

Figure 8. Total radial stress and excess pore pressure at the cavity wall.

The distribution of effective stresses and excess pore pressure at the end of cavity expansion are shown in Figure 9. There is a region near the cavity wall where both the numerical effective stresses do not change. The soil in this region is expected to be in critical states. Outside the critical state region, the effective radial stress exhibits a peak value at about r/a=6.0.

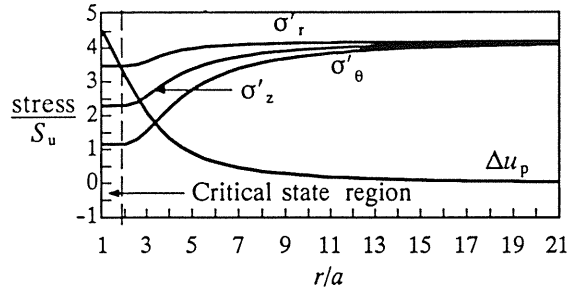

Figure 9. Distribution of effective stresses and excess pore pressure.

The total and effective stress paths for this problem are plotted in the p'-q diagram of Figure 10. The total and effective stress paths at different radial locations follow basically the same curves, but end at different positions. The effective stress path hits the critical state line at $q = 2S_u$. Once the critical state is reached, the effective stress path stays stationary and the total stress path moves parallel to the mean stress axis, which implies that any further increase in the total mean stress is completely balanced by the excess pore pressure.

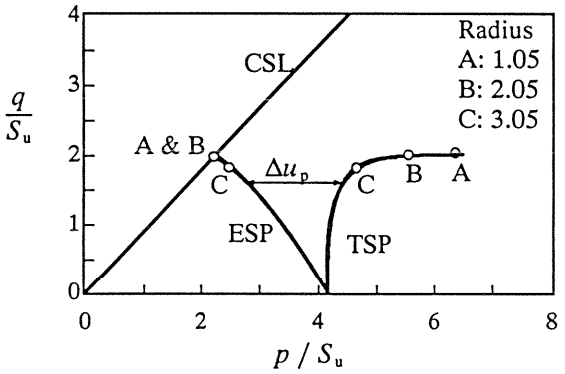

Figure 10. Effective and total stress paths.

4.3 Uncoupled analysis of rigid strip footing

The rigid strip footing problem is another good example for testing stress integration and load stepping methods. Due to the singularity at the edge of the footing and the strong rotation of the principal stresses, this case is difficult for Newton-Raphson and modified Newton-Raphson methods (see Gens and Potts, 1987). In this section, the modified Euler stress integration scheme and the automatic load stepping scheme are tested using the rigid strip footing problem.

Two constitutive models are used to simulate the subgrade soils, namely the modified Cam clay model (MCC) and the generalized Cam clay model (GCC). For the MCC model, the material parameters are

$M = 0.898, \lambda = 0.25, \varkappa = 0.05, \mu = 0.3, \gamma = 6$ kN/m^3

where the unit weight is for submerged soil. The critical state void ratio at $p' = 1$ is assumed to be 1.6 homogenously and the soil is assumed to be overconsolidated to 50 kPa at the ground surface.

The material parameters for the GCC model are the same as the for the MCC soil, with α (in equation (8)) being set to 0.77 so as to approximate the Mohr-Coulomb failure surface in the deviatoric plane. The parameter β' was fixed at 0.5.

The footing geometry and the element mesh are shown in Figure 11. The half width of the footing ($B/2$) is taken as 1 and a domain of 10 × 10 is divided into 288

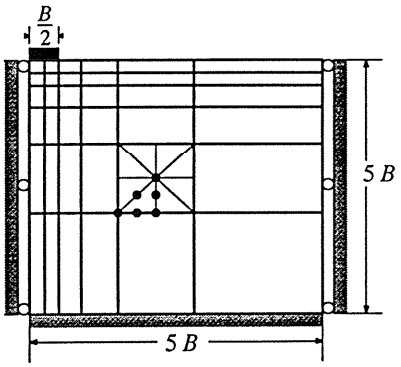

Figure 11. Mesh for footing analysis, 625 nodes, 288 elements and 1143 degrees of freedom.

triangular 6-noded triangles with a total of 1143 degrees of freedom. A total prescribed displacement of $0.2 \times B$ is applied to the footing in 50 coarse increments. An equivalent footing load is found by summing the appropriate nodal reactions.

The computed footing load-displacement curves for the both soil models are shown in Figure 12. For the MCC

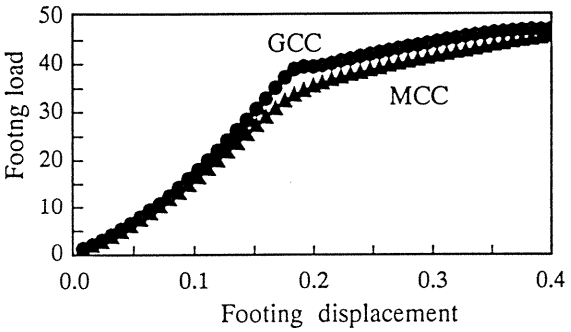

Figure 12. Footing load versus the footing displacement in uncoupled analysis.

soil, no obvious collapse load can be seen for the total displacement imposed (which is 40% of the half footing width). The footing load computed for the GCC model is slightly higher than that of the MCC model, probably due to the use of $\beta' = 0.5$, and asymptotes toward a limiting value at the end of the loading range.

The number of load subincrements in each coarse increment of prescribed displacement are plotted in Figure 13. Comparing this plot with Figure 12, we see that the number of load subincrements increases at turning points in material nonlinearity. At the start of loading, a relatively large number of load subincrements are needed due to the strongly nonlinear elastic behavior. These steadily decrease until local plastic yielding starts, where they then increase again. This result indicates that, without the automatic stepping method, it should be very difficult to determine the correct load increments. From Figure 13, it can also be seen that significant local failure occurs earlier in the GCC model than in the MCC model. This observation is consistent with the different shapes of the two failure surfaces in the deviatoric plane.

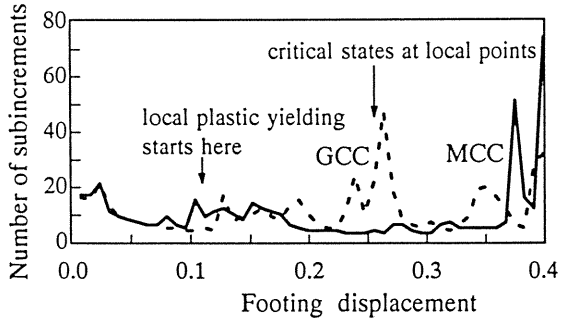

Figure 13. Number of load subincrements versus the footing displacement.

5. CONCLUSIONS

In this paper, a number of automatic solution schemes have been tested with two types of critical state models. The modified Euler method, described in Sloan et al (1998), has proved to be an efficient and reliable stress integration procedure. This confirms the general findings of Gens and Potts (1987) who concluded that explicit subincrementation techniques work well for complex soil models. For uncoupled problems, the automatic load incrementation algorithm of Abbo and Sloan (1996) provided a simple and robust method for performing accurate nonlinear finite element analysis. Similarly, the automatic time stepping scheme of Sloan and Abbo (1998) gave good results for coupled analysis of a variety of triaxial test cases and the undrained cavity expansion case. No numerical problems were encountered with any of the automatic schemes, which is a major attraction for practical computations.

As expected, the number of substeps in the automatic load-displacement integration was found to be highly sensitive to the local nature of the constitutive law. Without an automatic scheme, it would be difficult to determine a suitable series of load increments, even for a simple problem.

6. REFERENCES

Abbo, A.J. (1997), Finite Element Algorithms for Elastoplasticity and Consolidation, *PhD Thesis*, the University of Newcastle.

Abbo, A.J. & Sloan, S.W. (1996), An automatic load stepping algorithm with error control, *Int. J. Num. Meth. Eng.*, **39**, 1737-1759.

Carter, J.P., Randolph, M.F. & Wroth, C.P. (1979), Stress and pore pressure changes in clay during and after the expansion of a cylindrical cavity, *Int. J. Num. Anal. Meth. Geomechanics*, **3**, 305-322.

Collins, I.F. and Yu, H.S. (1996), Undrained cavity expansions in critical state soils, *Int. J. Num. Anal. Meth. Geomechanics*, **20**, 489-516, 1996.

Gens, A. & Potts, D.M. (1988), Critical state models in computational geomechanics, *Eng. Comp.* **5**, 178-197.

Naylor, D.J. (1975), Non-linear finite elements for soils, *PhD Thesis*, University of Swansea.

Roscoe, K.H. and Burland, J.B. (1968), On generalisation stress-strain behaviour of "wet" clay, *Engineering Plasticity*, Cambridge University Press, pp. 535-60.

Schofield, A.N. and Wroth, C.P. (1968), *Critical State Soil Mechanics*, McGraw-Hill, London.

Simpson, B. (1973), Finite element computations in soil mechanics, *PhD Thesis*, University of Cambridge.

Sloan, S.W. (1987), Substepping schemes for numerical integration of elastoplastic stress-strain relations, *Int. J. Num. Meth. in Eng.*, **24**, 893-911.

Sloan, S.W. & Abbo, A.J. (1998), An automatic time stepping scheme for elastic and elastoplastic consolidation. Part 1: Theory and implementation, Accepted by *Int. J. Num. Anal. Meth. Geomechanics*.

Sloan, S.W., Abbo, A.J. & Sheng, D. (1998), Explicit integration of elastoplastic models with error control, submitted to *Int. J. Num. Anal. Meth. Geomechanics*.

Yu, H.S. 1998), CASM: A unified state parameter model for clay and sand, *Int. J. Num. Anal. Meth. Geomechanics*, **22**, 621-653.

Zienkiewicz, O.C. & Pande, G.N. (1977), Some useful forms of isotropic yield surfaces for soil and rock mechanics, *Finite Elements in Geomechanics* (Ed. G. Gudehus), Chapter 5, John Wiley & Sons, Chichester.